Weierstraß-Institut
für Angewandte Analysis und Stochastik

Leibniz-Institut im Forschungsverbund Berlin e. V.

Preprint ISSN 2198-5855

Optical mode calculation in large-area photonic crystal surface-emitting lasers

Mindaugas Radziunas[1], Eduard Kuhn[1], Hans Wenzel[2], Ben King[2], Paul Crump[2]

submitted: December 21, 2023

[1] Weierstrass Institute
Mohrenstraße 39
10117 Berlin
Germany
E-Mail: mindaugas.radziunas@wias-berlin.de
eduard.kuhn@wias-berlin.de

[2] Ferdinand-Braun-Institut
Leibniz Institut für Höchstfrequenztechnik
Gustav-Kirchhoff-Straße 4
12489 Berlin
Germany
E-Mail: hans.wenzel@fbh-berlin.de
ben.king@fbh-berlin.de
paul.crump@fbh-berlin.de

No. 3075
Berlin 2023

2020 *Mathematics Subject Classification.* 78A60, 78-04, 78M20, 35L02, 65N25, 65Y04.

Key words and phrases. Semiconductor diode, PCSEL, photonic crystal, surface-emitting laser, modeling, optical modes, numerical algorithm, calculations.

This work was performed in the frame of the project “PCSELence” (K487/2022) funded by the German Leibniz Association.

Edited by
Weierstraß-Institut für Angewandte Analysis und Stochastik (WIAS)
Leibniz-Institut im Forschungsverbund Berlin e. V.
Mohrenstraße 39
10117 Berlin
Germany

Fax: +49 30 20372-303
E-Mail: preprint@wias-berlin.de
World Wide Web: http://www.wias-berlin.de/

Optical mode calculation in large-area photonic crystal surface-emitting lasers

Mindaugas Radziunas, Eduard Kuhn, Hans Wenzel, Ben King, Paul Crump

Abstract

We discuss algorithms and numerical challenges in constructing and resolving spectral problems for photonic crystal surface-emitting lasers (PCSELs) with photonic crystal layers and large (up to several tens of mm^2) emission areas. We show that finite difference schemes created using coarse numerical meshes provide sufficient accuracy for several major (lowest-threshold) modes of particular device designs. Our technique is applied to the example of large-area all-semiconductor PCSELs, showing how it can be used to optimize device performance.

1 Introduction

Semiconductor diode lasers are small, efficient, and relatively cheap devices compared to other lasers. Many applications require emission powers exceeding tens of watts from a single diode and up to a few kilowatts from a combined laser system [1]. Such emission can be achieved using high-power broad-area edge-emitting lasers (EELs) [2], which, unfortunately, have limitations. Although they remain the most efficient of all light sources, when operating at high power, the EEL emission is typically determined by multiple lateral modes and has a poor quality, i.e., it irregularly fluctuates in time (has a broad optical spectrum) and has large divergence, hardly improvable by external optical elements. In addition, the output facets of edge emitters require sophisticated facet passivation to suppress failures due to catastrophic optical mirror damage (COMD) and hence ensure long lifetimes, but at added cost and complexity [3].

In this work, we consider photonic crystal (PC) surface-emitting lasers (SELs), see Fig. 1, which, in contrast to EELs, can emit high-power (up to 80 W pulsed [4] and 50 W CW [5]) beams of nearly perfect quality in the (z) direction, perpendicular to the lateral (x/y) plain of the active material. Comparable to vertical cavity surface emitting lasers (VCSELs), the output surface of a PCSEL is a wide-bandgap crystalline GaAs-layer, so that COMD is not an issue and facet passivation is unnecessary.

Like VCSELs, PCSELs are sandwiched from multiple thin material layers along the vertical (z) direction, see Fig. 1(a), most of which are uniform in lateral directions. However, other than VCSEL, a properly designed PCSEL explores the two-dimensional band-edge resonant effect of the PC to select a single stable longitudinal and transverse mode that induces coherent large-area lasing. The critical part of the PCSEL, enabling an efficient coupling of counter- and cross-propagating optical fields generated within the active layer and their redirection along the z axis, is a-periodic in both lateral directions PC layer. For achieving field emission in the vertical direction, the lattice constant a must be closely related to the ratio of the central wavelength λ_0 and the effective index n_{eff} of the whole PCSEL, $a \approx \lambda_0/n_{\text{eff}}$. Moreover, for high outcoupling from a chosen surface (here, via the n-doped substrate), PCSELs require a backside reflector (e.g., Bragg grating, see Fig. 1(a)) to recycle part of light outcoupled into the opposite direction to the emission surface.

DOI 10.20347/WIAS.PREPRINT.3075 Berlin 2023

Each $a \times a$ unit cell of the PC has one or several features (e.g., triangles in Fig. 1(c)); materials inside and outside these features have different refractive indices. In simple cases, the PC layer is vertically homogeneous. In more complex cases, this layer can have several sublayers (e.g., three sublayers in Fig. 1(b)), and the 3-dimensional PC features should not necessarily have perpendicular side walls. Multiple sublayer cases can be designed intentionally or arise due to, e.g., imperfect material etching/regrowth procedure; see a schematic of such PC unitary cell in Fig. 1(d). Note that only the 2nd, 4th, and 6th sublayers in this diagram contain PC features that have the same shape, size, and position but are filled with different materials. PC layers containing vertically inhomogeneous features can also be treated as a composition of several vertically homogeneous layers; see, e.g., schematic cross-section of a tapered feature [6] in Fig. 1(e) or a top-view of such a feature at three different sublayers in Fig. 1(c).

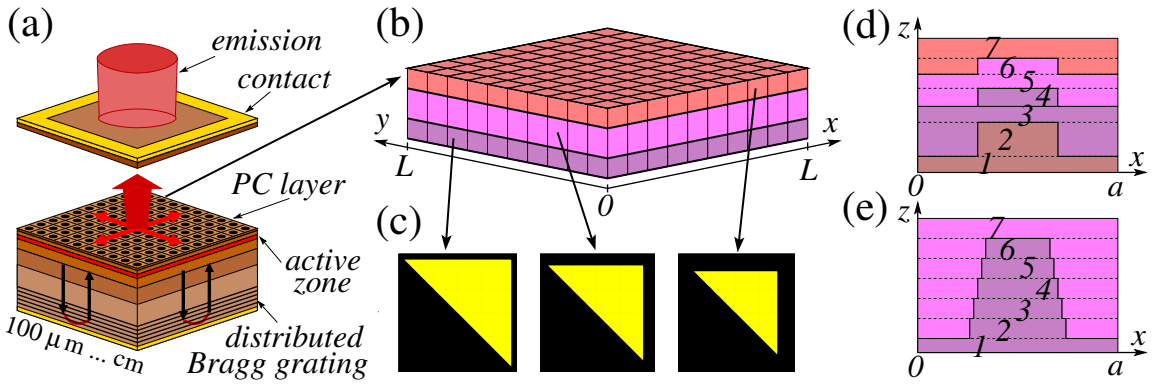

Figure 1: Schematic depiction of exemplary PCSEL (a) with the PC layer consisting of three vertically homogeneous sublayers (b) and different features within the PC unit cell in these sublayers (c). (d) and (e): schematic of the PC sublayers in vertical crosssections of the unit cell.

The periodic features of the PC layer in the highest power PCSELs reported up to date are filled with air, which guarantees a large refractive index contrast and, thus, a large coupling of optical fields within the PC. This high index contrast yields well-centered main modes already in moderate ($\sim 0.1\,\mathrm{mm}^2$) emission area PCSELs [7] so are very well suited to the realization of compact devices with output up to the watt-class, for example for application in short-reach pulsed LIDAR. For power scaling, much larger area PCSELs are needed, to enable sufficient heat extraction. Scaling to optical output powers into levels as high as kilowatts is estimated to require the use of very large apertures with many millimeters in cross section [8], to enable sufficient cooling. Proper numerical tools to handle PC structures of such large sizes require more efficient numerical algorithms, and these are the subject of the presented work. Specifically, this paper aims to present algorithms and numerical methods for the construction and numerical resolution of the spectral problem and discuss calculation-induced numerical errors. We illustrate the capability of the numerical tool using a low-index contrast PCSEL design, that is fabricated using an established right-angle triangle PC arrangement, taken from Ref. [8].

In Section 2, we present and briefly explain the derivation of the field equations of the dynamic three-dimensional coupled wave model and introduce the related spectral problem used for calculations of optical modes that can be excited close to the lasing threshold. Section 3 discusses the algorithms used to derive nontrivial complex field coupling matrix and the numerical challenges arising during the derivation. Section 4 introduces finite-difference schemes for solving the spectral problem and discusses their performance in dependence on the numerical mesh step. Section 5 gives a couple of examples showing the dependence of the leading optical mode relations on the size of the PCSEL. Conclusions and outlook are presented in Section 6.

2 Model

2.1 Field equations

We exploit a three-dimensional coupled-wave model [9, 10], derived from Maxwell's equations using lateral Fourier expansions of the dielectric constant $\tilde{n}^2(\mathbf{r},t) = n_S^2(\mathbf{r}) + \delta_n^2(z,N,T)$ and TE-polarized electrical field $\mathbf{E}(\mathbf{r},t) = (E_x, E_y, 0)^T$ to model large emission area ($\gg 0.1\,\mathrm{mm}^2$) PCSELs. The real-valued $n_S^2(\mathbf{r})$ represents (real) material indices in the cold-cavity PCSEL. It accounts for tiny periodic structures of the PC layers, see, e.g., Fig. 2(a), and is laterally uniform in the remaining PCSEL layers. δ_n^2 also accounts for small-scale laterally averaged field losses in all material layers (defined by non-vanishing imaginary parts of corresponding dielectric constants), losses within the active material, and gain and refractive index change induced by the carrier density N and temperature T. The field equations are formulated for along lateral directions counterpropagating complex, slowly varying field amplitudes $u^{\pm}(x,y,t)$ and $v^{\pm}(x,y,t)$, which, after multiplication by the vertical mode function $\Theta(z)$, are proportional to the electrical field Fourier components $E_{y,\pm1,0}$ and $E_{x,0,\pm1}$ at the rapidly oscillating harmonics $\exp(i(\omega_0 t \mp \beta_0 x))$ and $\exp(i(\omega_0 t \mp \beta_0 y))$, respectively. By scaling of $u^{\pm}$ and $v^{\pm}$, $\sum_{\nu=\pm}(|u^{\nu}|^2+|v^{\nu}|^2)$ is a local two-dimensional photon density. The amplitudes $u = \binom{u^+}{u^-}$ and $v = \binom{v^+}{v^-}$ evolve according to the 1(time)+2(space) dimensional partial differential equations

$$\frac{i}{v_g}\frac{\partial}{\partial t}\begin{pmatrix}u\\v\end{pmatrix} = \mathcal{H}(\Delta\beta)\begin{pmatrix}u\\v\end{pmatrix} + F_{sp},\ (x,y)\in[0,L]\times[0,L], \tag{1a}$$

$$u^+(0,y) = u^-(L,y) = v^+(x,0) = v^-(x,L) = 0, \tag{1b}$$

$$\mathcal{H}(\Delta\beta) = \Delta\beta - i\begin{pmatrix}\sigma\frac{\partial}{\partial x} & \mathbf{0}\\ \mathbf{0} & \sigma\frac{\partial}{\partial y}\end{pmatrix} - \mathbf{C},\ \sigma = \begin{pmatrix}1 & 0\\ 0 & -1\end{pmatrix}, \tag{1c}$$

$$\Delta\beta = \frac{\beta^2-\beta_0^2}{2\beta_0} + \frac{k_0^2}{2\beta_0}\int \delta_n^2(z,N,T)|\Theta(z)|^2 dz. \tag{1d}$$

L, F_{sp}, and v_g in (1a) denote the lateral dimension of the PCSEL, the Langevin noise source vector, and the group velocity. Boundary conditions (1b) suggest no reflections (i.e., full absorption) of the fields escaping through the lateral bounds of the domain, but can be easily modified, allowing non-vanishing reflections at the borders. Eq. (1c) shows the structure of the operator $\mathcal{H}$, which depends on the complex 4×4 field coupling matrix $\mathbf{C}$ and relative complex propagation factor $\Delta\beta(x,y,t)$ defined in (1d). Here, $k_0 = 2\pi/\lambda_0$ and $\beta_0 = 2\pi/a$ are the central and the Bragg wavevectors, respectively. $\beta = k_0 n_{\mathrm{eff}} \approx \beta_0$ is the propagation factor defined by the effective refractive index n_{eff}, which, together with Θ (black-dashed and violet lines in Fig. 2(c)), can be found by solving one-dimensional Helmholtz problem

$$\Big[\frac{d^2}{dz^2} + k_0^2(n_0^2(z) - n_{\mathrm{eff}}^2)\Big]\Theta(z) = 0,\ \int|\Theta|^2 dz = 1, \tag{2a}$$

$$\Big[\frac{d}{dz} - \sigma_b\Big]\Theta(z=0) = \Big[\frac{d}{dz} + \sigma_t\Big]\Theta(z=L_z) = 0, \tag{2b}$$

$$\sigma_j = k_0\sqrt{n_{\mathrm{eff}}^2 - n_j^2},\quad \Re\sigma_j \geq 0,\quad j\in\{b,t\}, \tag{2c}$$

where $z = 0$ and $z = L_z$ are the bottom and top sides of the PCSEL, whereas n_b and n_t are (in general, complex) refractive indices of media behind these borders. Real-valued function $n_0^2(z)$ in Eq. (2) (red dots in Fig. 2(c)) is a PC cell-wise lateral average of $n_S^2(\mathbf{r})$: $n_0^2(z) = \langle n_S^2\rangle_a = \frac{1}{a^2}\iint_{-a/2}^{a/2} n_S^2(\mathbf{r})dxdy$. A detailed knowledge of $n_S^2(\mathbf{r})$, $n_0^2(z)$, and $\Theta(z)$, all shown in Fig. 2(a) and (c), is also needed to construct the coupling matrix $\mathbf{C}$, which will be discussed in Section 3.

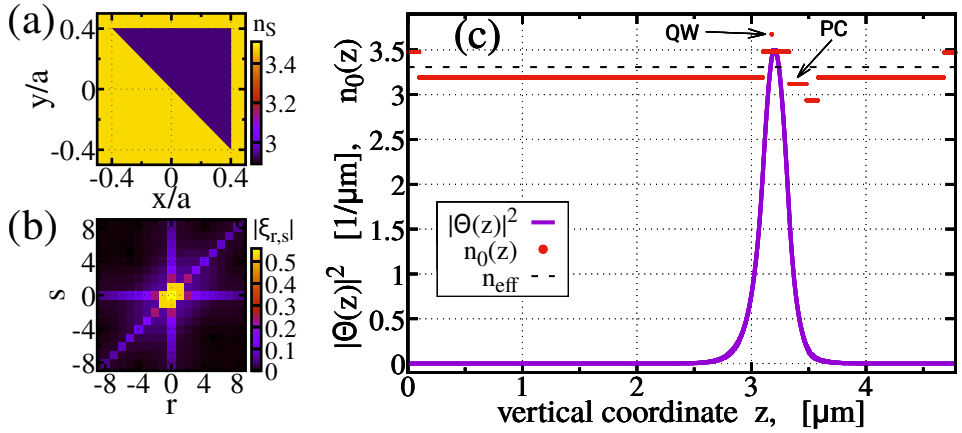

Figure 2: Structure of the considered PCSEL example. (a): Refractive index $n_S(\mathbf{r})$ within the PC cell. (b): Several factors $|\xi_{r,s}|$ for $|r|+|s|>0$. (c): Function $n_0(z)$ (red), corresponding n_{eff} (black dashed), and vertical mode intensity $|\Theta|^2$ (violet).

2.2 Spectral problem

In general, the field equations (1) should be supplemented with the model for $\delta_n^2(z,N,T)$, see, e.g., Ref. [11], and models accounting for dynamics of carrier density N [10, 11] and temperature distribution T [12]. This paper considers PCSELs where $\Delta\beta$ remains stationary in time. For example, once operating close to the lasing threshold, $\Delta\beta$ remains time-independent and (nearly) uniform in space, such that it can be well represented by a single complex constant $\overline{\Delta\beta}$. By substituting $\binom{u}{v} = \Phi(x,y)e^{i\tilde{\omega}t}$ into Eqs. (1), we get the spectral problem [9]

$$\left[\mathbf{C}+i\begin{pmatrix}\sigma\frac{\partial}{\partial x} & \mathbf{0}\\ \mathbf{0} & \sigma\frac{\partial}{\partial y}\end{pmatrix}\right]\Phi = \Omega\Phi,\ (x,y)\in[0,L]\times[0,L], \tag{3a}$$

$$\Phi_u^+(0,y) = \Phi_u^-(L,y) = \Phi_v^+(x,0) = \Phi_v^-(x,L) = 0, \tag{3b}$$

$$\Omega = \Delta\beta + \frac{\tilde{\omega}}{v_g},\ \ \|\Phi\|^2 = \iint_0^L |\Phi(x,y)|^2 dxdy = 1. \tag{3c}$$

Here, $|\Phi(x,y)|^2 = \Phi^*\cdot\Phi$ is a real-valued mode intensity distribution function, whereas $\|\xi\|^2$ and later used (ξ,ζ) denote the squared norm and the standard scalar product of four-component vector functions. Eqs. (3) define ($\Delta\beta$-dependent) optical modes $(\tilde{\omega},\Phi(x,y))$ [13], with $\tilde{\omega}$ and $\Phi(x,y) = \binom{\Phi_u}{\Phi_v}$ denoting complex frequency and scaled four-component distribution of the mode, respectively. Positive and negative $\Im\tilde{\omega}$ indicate exponential damping or amplification of the modes, whereas the mode with constant in time amplitude should have $\Im\tilde{\omega}=0$. When the PCSEL is not lasing, all modes are damped, $\Im\tilde{\omega}>0$. The complex frequency $\tilde{\omega}$ enters the spectral problem together with the propagation factor $\Delta\beta$, whose imaginary part, $\Im\Delta\beta = \frac{g-\alpha_0}{2}$, is determined by the gain g and internal field losses α_0. Like $\Delta\beta$, the factor Ω in Eq. (3c) is, in general, a complex spatially distributed function and, thus, can not be directly treated as the eigenvalue (or scaled eigenfrequency) of the problem (3a), (3b). In the close-to-threshold case, when $\Delta\beta = \overline{\Delta\beta}$, however, Ω is a complex constant depending only on the field coupling matrix $\mathbf{C}$ (defined by the heterostructure of the cold cavity PCSEL) and the lateral size factor L. Real and imaginary parts of Ω, $\Re\Omega$ and $\Im\Omega$, represent frequency detuning from the Bragg condition and the gain required for the corresponding mode to reach its threshold [9] (i.e., $\Im\tilde{\omega}=0$).[1] Thus, complex eigenfrequencies Ω with low $\Im\Omega$ are crucial in selecting PCSEL het-

[1] Mode threshold $\Im\Omega = \Im\Delta\beta$ also includes a field loss term. If this loss is constant, it gives only a correcting up-shift of the mode threshold gain value.

erostructures. Finding several major (low-threshold) modes allows for predicting the lasing threshold and estimating the side mode suppression (damping) in the close-to-threshold operating state. While $\Im\Delta\beta$ of just switched-on laser remains fixed by $\Im\Omega_1$, the threshold gap $\Im(\Omega_j - \Omega_1) = \frac{\Im\tilde{\omega}_j}{v_g}$, $j > 1$, defines damping of higher order modes. Additional information on the quality of each mode at its threshold can be obtained from the integral relation [9] derived using the scalar product of Eqs. (3a) with Θ^*:

$$\begin{aligned} g &= \alpha_0 + \alpha_\mathrm{e} + g_\mathrm{r}, \qquad g_\mathrm{r} = 2\Im(\Phi, \mathbf{C}_\mathrm{rad}\Phi), \\ \alpha_\mathrm{e} &= \textstyle\int_0^L |\Phi_u^+(L,y)|^2 + |\Phi_u^-(0,y)|^2 dy \\ &\quad + \int_0^L |\Phi_v^+(x,L)|^2 + |\Phi_v^-(x,0)|^2 dx. \end{aligned} \tag{4}$$

Here, g_r is part of the gain used for the field outcoupling into the vertical direction, $\mathbf{C}_\mathrm{rad}$ is by the radiative field components $E_{x/y,0,0}$ induced contribution to matrix $\mathbf{C}$, and the loss factor α_e represents the fields escaping through the lateral borders.

3 Coupling matrix C

3.1 Construction of the coupling matrix

To complete the construction of the model equations (1) and (3), one still has to define the coupling matrix $\mathbf{C}$, which is a a combination of the following set of parameters [9, 10]:

$$\xi_{r,s}^{(j)} = \xi_{r,s}(z)|_{z\in S_j} = \langle n_S^2(x,y,z)|_{z\in S_j} e^{i\beta_0(rx+sy)}\rangle_a, \tag{5a}$$

$$\mathcal{P}^{(j)} = \int_{S_j} |\Theta(z)|^2 dz, \tag{5b}$$

$$\mathcal{G}_{(r,s)}^{(k,j)} = \int_{S_k} \Theta^*(z) \int_{S_j} G_{(r,s)}(z,z')\Theta(z')dz'dz. \tag{5c}$$

Here, r and s belong to the infinite set of integer numbers, whereas the indices k and j represent the finite set of material layers S_k and S_j. $\xi_{r,s}(z)$ in Eq. (5a) are Fourier coefficients of the function $n_S^2(\mathbf{r}) = \sum_{r,s}\xi_{r,s}(z)e^{-i\beta_0(rx+sy)}$, see, e.g., red dots in Figs. 2(c) and Fig. 2(b), representing $n_0(z) = \sqrt{\xi_{0,0}(z)}$ in all layers and $|\xi_{r,s}(z)|$ of several most essential coefficients within the single PC layer, respectively. For the real-valued n_S^2, we have $\xi_{-r,-s} = \xi_{r,s}^*$. Like $n_S^2(\mathbf{r})$, $\xi_{r,s}$ are layer-wise constant functions of z and, thus, can be represented by a finite set of complex constants $\xi_{r,s}^{(j)}$. $\mathcal{P}^{(j)}$ in Eq. (5b) represents part of the vertical mode intensity within the material layer S_j. Factors $\mathcal{G}_p^{(k,j)}$ with $p = (r,s)$, $|p| = \sqrt{r^2+s^2} \neq 1$ in Eq. (5c) are obtained by integrating the expressions involving Green's function $G_p(z,z')$, which solves the inhomogeneous problem

$$\begin{aligned} &\left[\tfrac{\partial^2}{\partial z^2} + k_0^2 n_0^2(z) - \beta_0^2|p|^2\right] G_p(z,z') = -\delta(z-z'), \\ &\left[\tfrac{\partial}{\partial z} - \sigma_{p,b}\right] G_p(0,z') = \left[\tfrac{\partial}{\partial z} + \sigma_{p,t}\right] G_p(L_z,z') = 0, \\ &\sigma_{p,j} = k_0\sqrt{\beta_0^2|p|^2 - k_0^2 n_j^2}, \quad \Re\sigma_{p,j} \geq 0,\ j \in \{b,t\}. \end{aligned} \tag{6}$$

For real-valued n_j and $|p| = 0$, $\Re\sigma_{0,j}$ in Eq. (6) vanishes, meaning that the tails of $G_p(z,z')$ are fixed-amplitude oscillations when $z \to \pm\infty$. We use $\sigma_{0,j} = i|\sigma_{0,j}|$, which reminds us of Sommerfeld's radiation conditions, even though those are formulated only for two- and three-dimensional cases.

The Fourier coefficients $\xi_{r,s}^{(j)}$ with $|r| + |s| \neq 0$ are non-vanishing only when S_j is a PC sublayer. Since these coefficients are only used as multipliers of the factors $\mathcal{P}^{(j)}$ and $\mathcal{G}_p^{(k,j)}$ or $\mathcal{G}_p^{(j,k)}$, we should

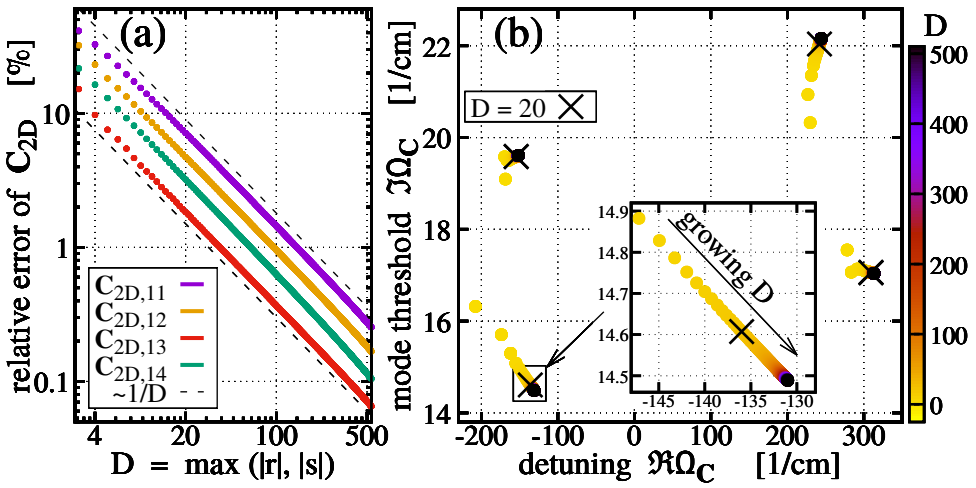

Figure 3: Calculations of $\mathbf{C}$ using different truncation parameters D. (a): Relative error of $\mathbf{C}_{2D}^{(D)}$ elements as function of D, decaying as $1/D$ with growing D. (b): spectrum of $\mathbf{C}$ in dependence on D. Crosses show eigenfrequencies of $\mathbf{C}$ obtained using $D = 20$.

calculate $\mathcal{P}^{(j)}$ and $\mathcal{G}_p^{(k,j)}$ only for those indices k, j which correspond to the PC sublayers. For the formulas defining $\mathbf{C}$ as function of $\xi_{r,s}$, $\mathcal{P}$, and $\mathcal{G}_p$, see Refs. [9, 10]. The algorithms for optimizing the matrix $\mathbf{C}$ and its eigenfrequencies by selecting the PC configuration and, thus, tailoring the set of coefficients $\xi_{r,s}$ were discussed in Ref. [8]. This work briefly introduces the algorithms used to calculate $\mathcal{P}^{(j)}$ and $\mathcal{G}_p^{(k,j)}$ and the challenges arising during these calculations [14]. For a mathematically rigorous description of these algorithms, see Ref. [15].

Typically, $\mathbf{C}$ is written as a sum of a non-hermitian matrix $\mathbf{C}_{\text{rad}}(\mathcal{G}_{(0,0)}, \xi_{\pm1,0}, \xi_{0,\pm1})$ (out-of-plane coupling via radiative waves), and two Hermitian matrices $\mathbf{C}_{1D}(\mathcal{P}, \xi_{\pm2,0}, \xi_{0,\pm2})$ (coupling of counterpropagating waves) and $\mathbf{C}_{2D}$ (2D coupling via higher order, $|m| + |n| > 1$, modes). The Hermitian nature of the last two matrices, which is because $n_s^2(\mathbf{r})$, $\mathcal{P}^{(j)}$, and $\mathcal{G}_p^{(k,j)}$ for $|p| > 1$ are real-valued, is explored when calculating the fields at the upper or lower edges of the PCSEL, for example. Small imaginary dielectric constant contributions in cold cavity PCSEL ignored when constructing $\mathbf{C}$ should be included into δ_n and, thus, $\Delta\beta$.

The last matrix $\mathbf{C}_{2D}$ is an infinite sum,

$$\mathbf{C}_{2D} = \sum_{|r|+|s|>1} \mathbf{C}_{2D}^{(r,s)}(\mathcal{P}, \mathcal{G}_{(r,s)}, \xi_{r\pm1,s}, \xi_{r,s\pm1}). \tag{7}$$

In our calculations, we truncate this sum, i.e., replace $\mathbf{C}_{2D}$ with $\mathbf{C}_{2D}^{(D)}$, which accounts only for parameter sets (r, s) with $\{|r|, |s|\} \leq D$ [16]. Fig. 3, which explores the PCSEL configuration defined by the multiple material layers with indices $n_0(z)$, see Fig. 2(c), and the PC cells containing isosceles right triangle features with leg lengths of $0.8a$, Fig. 2(a), shows a typical relatively slow convergence of calculations with growing D. Panel (a) of this figure shows a $(1/D)$-type decay of the relative errors $\frac{|\mathbf{C}_{2D,ij}^{(D)} - \mathbf{C}_{2D,ij}|}{|\mathbf{C}_{2D,ij}|}$ of four well-distinguishable matrix elements with increasing D. An unknown exact matrix $\mathbf{C}_{2D}$ was substituted by $\mathbf{C}_{2D}^{(1000)}$ in the relative error estimates. At $D \sim 150$, these errors are below 1%, and adding further terms induces only minor changes of $\mathbf{C}$. Another representation of this convergence is given in Fig. 3(b), where changes of four eigenfrequencies $\Omega_{\mathbf{C}}$ of the matrix $\mathbf{C}$ (each corresponding to one of the band-edge modes of the infinitely broad PCSEL) with an up-sweep of D (yellow: small D, dark: large D) are shown. Since we explore analytic formulas [15] for constructing

$\mathbf{C}$, matrix calculations using $D = 500$ in the presented case could be done in only 20 seconds on a standard notebook. Note that this time includes not only an estimation of $\mathbf{C}_{2D}$ but also reading and reorganization of the input parameters, 2D-Fourier transform of $n_S^2(\mathbf{r})$ within the PC layer, solution of the Helmholtz problem (2), and calculation of the factors $\mathcal{P}$, matrices $\mathbf{C}_{1D}$, and $\mathbf{C}_{\text{rad}}$. However, the time needed for estimation of $\mathbf{C}_{2D}$ grows nearly quadratically with the increasing number of PC sublayers, such that using relatively small D can be an attractive option when fast estimation of $\mathbf{C}$ is essential. Matrices constructed using $D = 20$ and $D = 500$ are explored in example simulations in the remainder of the paper. Even though $\Omega_{\mathbf{C}}$ calculated with $D = 20$ is still apart from the final position, see the inset of Fig. 3(b), this D can be sufficient for practical calculations. Estimation of $\mathbf{C}$ using $D = 20$ and fully numerical procedures for $\mathcal{G}_p^{(k,j)}$ and $\mathcal{P}^{(j)}$ in PCSELs with multilayer PCs are less precise and can take hours and even days.

3.2 Numerical algorithms

To solve the Helmholtz problem (2), we replace it with a characteristic equation constructed using transfer matrices [17]. Within each material layer S_j, functions $\Theta(z)$ satisfying Eq. (2a) and their derivatives $\frac{d}{dz}\Theta(z)$ can be written as linear combinations of $e^{\sigma_j(z-z_j)}$ and $e^{\sigma_j(z_{j-1}-z)}$, where $z_{j-1} = z_j - |S_j|$, z_j, and $|S_j|$ are two edges and thickness of the layer S_j, while $\sigma_j = k_0\sqrt{n_{\text{eff}}^2 - n_0^2|_{z\in S_j}}$ with $\Re\sigma_j \geq 0$. Thus, provided n_{eff} and $\Theta(z)$ at the edges of S_j are known, the field intensity factor $\mathcal{P}^{(j)}$ can be written using analytic formulas. When n_{eff} is not known, $e^{\pm\sigma_j|S_j|}$ can be interpreted as functions of the variable $n_\bullet$. We use them to construct 2×2-transfer matrices $\mathbf{M}_j(n_\bullet)$, translating vector $V(z) = (\Theta, \frac{d}{dz}\Theta)^T$ across material layers S_j. The consequent product of these matrices built for all layers gives us an overall transfer matrix $\mathbf{M}(n_\bullet)$, translating $V(z)$ from $z = 0$ up to $z = L_z$, where both components of V are related by Robin-type boundary conditions (2b), and $\sigma_{b,t}$ are functions of $n_\bullet$. The complex characteristic equation reads as $\chi(n_\bullet) = (\sigma_t, 1)\mathbf{M}\left(\begin{smallmatrix}1\\ \sigma_b\end{smallmatrix}\right) = 0$.[2] For real n_0, the roots $n_\bullet$ are also real and are located between maximal and minimal $n_0(z)$. We find these roots using Newton iterations, exploring analytic formulas for $\chi(\xi)$ and $\frac{d}{d\xi}\chi(\xi)$. For each root $n_\bullet$, we reconstruct related $\Theta(z)$ using transfer matrices. The mode with the largest intensity within the QW and PC layers is the main vertical mode $\Theta(z)$, and a corresponding $n_\bullet$ is the effective index n_{eff}. For more details, see Ref. [15].

For some structures, exponentials $e^{\Re\sigma_j|S_j|}$ can be huge, such that evaluation of $\mathbf{M}_j(\xi)$ and $\chi(\xi)$ using the first version of our code was impossible. To solve this computer-arithmetic-related problem [18], we introduced bounded matrices $\widetilde{\mathbf{M}}_j = \mathbf{M}_j e^{-\sigma_j|S_j|}$ and explored them to construct the characteristic function. An example of calculated vertical mode, the corresponding function $n_0(z)$ and n_{eff}, is given in Fig. 2(c).

In Ref. [15], we also demonstrated that for any $(z, z') \in S_k \times S_j$, the Green's function $G_p(z, z')$ can be written as

$$
\begin{aligned}
G_p &= \begin{cases} \frac{e^{-\sigma_{p,j}|z-z'|}}{2\sigma_{p,j}} + \mathcal{E}_{p,j}^T(z')\mathbf{B}_{p,j}\mathcal{E}_{p,j}(z) & k = j \\ \mathcal{E}_{p,j}^T(z')\mathbf{A}_{p,k}^j\mathcal{E}_{p,k}(z) & k \neq j \end{cases}, \\
\mathcal{E}_{p,j}(\zeta) &= \tfrac{2}{1+e^{-\sigma_{p,j}|S_j|}}\begin{pmatrix} e^{\sigma_{p,j}(\zeta-z_j)} \\ e^{\sigma_{p,j}(z_{j-1}-\zeta)}\end{pmatrix}, \\
\sigma_{p,j} &= \sqrt{\beta_0^2|p|^2 - k_0^2 n_0^2(z)}, \qquad \Re\sigma_{p,j} \geq 0,
\end{aligned}
\tag{8}
$$

where $\mathbf{B}_{p,j}$ and $\mathbf{A}_{p,k}^j$ are 2×2 constant matrices, which can be calculated using analytic expressions.

[2] For Dirichlet boundary conditions used in the example of Fig. 2, $[\partial_z \mp \sigma_{b,t}]$ in Eq. (2b) are replaced by 1, and the characteristic function is $\chi = \mathbf{M}_{21}(n_\bullet)$.

Since $\Theta^*(z)G_p(z,z')\Theta(z')$ for $(z,z') \in S_k \times S_j$ is given by a linear combination of exponentials, the integral factors $\mathcal{G}_p^{(k,j)}$ in Eq. (5c) can also be expressed by analytic formulas.

We fixed $z' \in S_j$ and used the homogeneity of Eq. (6) for $z < z'$ and $z > z'$ to derive these formulas. Within each S_k, $k \neq j$, the transfer matrices $\widetilde{\mathbf{M}}_{p,k}$ (built using $\sigma_{p,k}$ instead of σ_k) translate Robin-type boundary conditions between the edges of the layer. Thus, we can translate these conditions defined by $\sigma_{p,b}$ and $\sigma_{p,t}$ in Eq. (6) from $z = 0$ to z_{j-1} and form $z = L_z$ to z_j, obtaining (z'-independent) factors $\eta_{p,b}^{(j)}$ and $\eta_{p,t}^{(j)}$, respectively. Similarly, we build z'-dependent transfer matrices $\widetilde{\mathbf{M}}_{p,j}^{+}$ and $\widetilde{\mathbf{M}}_{p,j}^{-}$ translating the vector $(G_p, \partial_z G_p)^T$ from z_{j-1} to $z' - 0$ and from z_j to $z' + 0$. These matrices, Robin-type conditions at the edges of S_j, continuity of G_p, and δ-function induced jump down by 1 of $\partial_z G_p$ at $z = z'$ imply the following system of two inhomogeneous linear equations:

$$\widetilde{\mathbf{M}}_{p,j}^{+}\begin{pmatrix}1\\ \eta_{p,b}^{(j)}\end{pmatrix}G_p(z_{j-1},z') + \widetilde{\mathbf{M}}_{p,j}^{-}\begin{pmatrix}-1\\ \eta_{p,t}^{(j)}\end{pmatrix}G_p(z_j,z') = \begin{pmatrix}0\\ 1\end{pmatrix}.$$

The formulas for constant matrix $\mathbf{B}_{p,j}$ in Eq. (8) directly follow from the z'-dependent expressions of $G_p(z_{j-1}, z')$ and $G_p(z_j, z')$. Translation of the Robin-type conditions at z_{j-1} and z_j over S_k, $k \neq j$, allows a quick calculation of $G_p(z, z')$ at the remaining material interfaces, which are sufficient for deriving formulas for matrices $\mathbf{A}_{p,k}^{j}$ in Eq. (8).

Notably, analytic formulas representing $G_{r,s}$ and related double integrals $\mathcal{G}_{(r,s)}^{(k,j)}$ for large $|r|$ and $|s|$ can imply floating-number-arithmetic-related problems [18] since we must handle very large and small exponentials $e^{\pm\sqrt{r^2+s^2}\beta_0 z}$. Our first simulations using built-in $\sinh$ and $\cosh$ functions within transfer matrices failed at $D = 25$. By treating large and small exponentials separately (i.e., replacing possibly huge matrices $\mathbf{M}_{p,j}$ with bounded matrices $\widetilde{\mathbf{M}}_{p,j}$) and avoiding division of very large and small numbers, we could run calculations up to $D \approx 200$. After accounting for further computer-arithmetic problems (such as $\varepsilon + 1 - 1 \equiv 0$ whereas $\varepsilon + (1 - 1) \equiv \varepsilon$ for $|\varepsilon| < 10^{-16}$), we could use much larger D: see, e.g., Fig. 3, where calculations were performed up to $D = 510$.

4 Solution of the spectral problem

4.1 Finite difference scheme

Let us return to the solution of the spectral problem (3). Since we cannot resolve this problem analytically, we rely on fully numerical procedures and finite difference schemes, and instead of vector functions $\Phi(x, y)$ and eigenfrequencies Ω, we look for their discrete analogs Φ^h and Ω_h, which for properly constructed schemes should provide good approximations of the original values. The domain $[0, L] \times [0, L]$ is discretized to q^2 equal small squares (cells) with the edge length $h = \frac{L}{q}$. Each of the four model equations (3a) is approximated in the center of each such cell, i.e., at q^2 positions $(x_r, y_s) = ((r - 0.5)h, (s - 0.5)h)$, $r, s \in \{1, \ldots, q\}$. We introduce the mesh function Φ^h with elements $\Phi^{h\pm}_{u,r,s-0.5}$ (including $r = 0$) and $\Phi^{h\pm}_{v,r-0.5,s}$ (including $s = 0$), which approximate original continuous functions $\Phi_u^{\pm}$ and $\Phi_v^{\pm}$ at $(rh, (s-0.5)h)$ and $((r-0.5)h, sh)$, i.e., at the center of vertical and horizontal edges of all cells, respectively. Overall, this mesh function Φ^h has $4q(q + 1)$ unknown complex elements. Or, more exactly, $4q^2$ unknown elements, since due to Eq. (3b), $4q$ variables at the edges of the whole domain should be zeros. A simple central finite difference scheme, consisting of

$4q^2$ linear equations and constructed using two-point stencils, is realized by substituting

$$\begin{aligned}
\Phi_u^{\pm}(x_r, y_s) &= \tfrac{\Phi^{h\pm}_{u,r,s-0.5}+\Phi^{h\pm}_{u,r-1,s-0.5}}{2} + \mathcal{O}(h^2),\\
\partial_x\Phi_u^{\pm}(x_r, y_s) &= \tfrac{\Phi^{h\pm}_{u,r,s-0.5}-\Phi^{h\pm}_{u,r-1,s-0.5}}{h} + \mathcal{O}(h^2),\\
\Phi_v^{\pm}(x_r, y_s) &= \tfrac{\Phi^{h\pm}_{v,r-0.5,s}+\Phi^{h\pm}_{v,r-0.5,s-1}}{2} + \mathcal{O}(h^2),\\
\partial_y\Phi_v^{\pm}(x_r, y_s) &= \tfrac{\Phi^{h\pm}_{v,r-0.5,s}-\Phi^{h\pm}_{v,r-0.5,s-1}}{h} + \mathcal{O}(h^2),
\end{aligned} \tag{9}$$

into Eqs. (3a) at each of q^2 positions (x_r, y_s). Terms $\mathcal{O}(h^2)$ in Eq. (9), obtained using Taylor's expansion of Φ at (x_r, y_s), show that our scheme is of second order (w.r.t. the small step h). We note that such scheme possesses a discrete version of the conservation law (4) [15] which we use to estimate the quality of the modes. After eliminating trivial boundary elements of Φ^h and ordering all elements of Φ^h into a single vector, we can write the resulting discrete spectral problem as

$$\mathbf{L}_h\Phi^h = \mathbf{D}_h\Omega_h\Phi^h \quad \Leftrightarrow \quad \mathbf{D}_h^{-1}\mathbf{L}_h\Phi^h = \Omega_h\Phi^h. \tag{10}$$

$\mathbf{L}_h$, $\mathbf{D}_h$ are complex $4q^2 \times 4q^2$ matrices, each having $\sim 32q^2$ and $\sim 8q^2$ non-vanishing elements. $\mathbf{D}_h$ is easily invertible; construction of $\mathbf{D}_h^{-1}\mathbf{L}_h$ requires only $4q^2$ arithmetic operations, but the matrix itself has $\sim 8q^3$ entries.

When simulating large PCSELs, which, in general, requires large q and, thus, substantial memory resources and processing time, one can use higher-order schemes. Redefinition of the mesh function Φ^h is not needed; the schemes in the discretized domain's larger (inner) part can be constructed using centered differences and straight 2ν-point stencils (2ν: order of the scheme). The drawback of such schemes is that at each of the $\nu - 1$ cell layers at the domain borders, one has to use $(2\nu + 1)$-point stencils and non-centered finite differences. Stil sparse matrices $\mathbf{D}_h$, $\mathbf{L}_h$ have additional nonzero entries, and, compared to the standard scheme, the solution of the same size problem (10) takes more time. A clear advantage is an enhanced precision in approximating several leading eigenfrequencies Ω, which can be achieved using moderate step h. Thus, if achieving good precision is essential, schemes with moderate h and $\nu > 1$ can be significantly faster, compared to the standard scheme (9) with much finer h.

4.2 Example

The (finite-dimensional) numerical scheme (10) does not approximate all (i.e., an infinite number of) modes of the original problem (3); the numerically induced error of mode approximation grows with an increasing mesh step h. For large-area PCSELs and moderate or small discretization steps (e.g, $L \geq 5\,$mm, $h = 10\,\mu$m, $q \geq 500$), Eq. (10) defines millions of modes, but not all of them can be found because of computer memory and time constraints. Fortunately, only a few modes are essential. Thus, we exploit the sparseness of the matrices and look only for a few dominant modes preselected in preliminary calculations with a coarse numerical mesh.

For the construction and solution of the discrete spectral problem (10), we used the Julia programming language (version 1.9) [19] and the available spectral solvers. The example calculations presented in Fig. 4 were performed using coupling matrix $\mathbf{C}$ from Fig. 3 estimated for $D = 20$ or 500. We assumed that $L = 1\,$mm and the PC lattice constant $a = \lambda_0/n_{\text{eff}}$ is defined by the central wavelength $\lambda_0 = 1.07\,\mu$m and the effective refractive index n_{eff} determined by Eq. (2). Light blue dots in Fig. 4(a) show only a small part of Ω_h calculated using $D = 20$ and $q = 48$. Five lowest threshold modes are represented by blue dots within the black ellipse in the inset of Fig. 4(a) and the diagrams of Fig. 4(c),

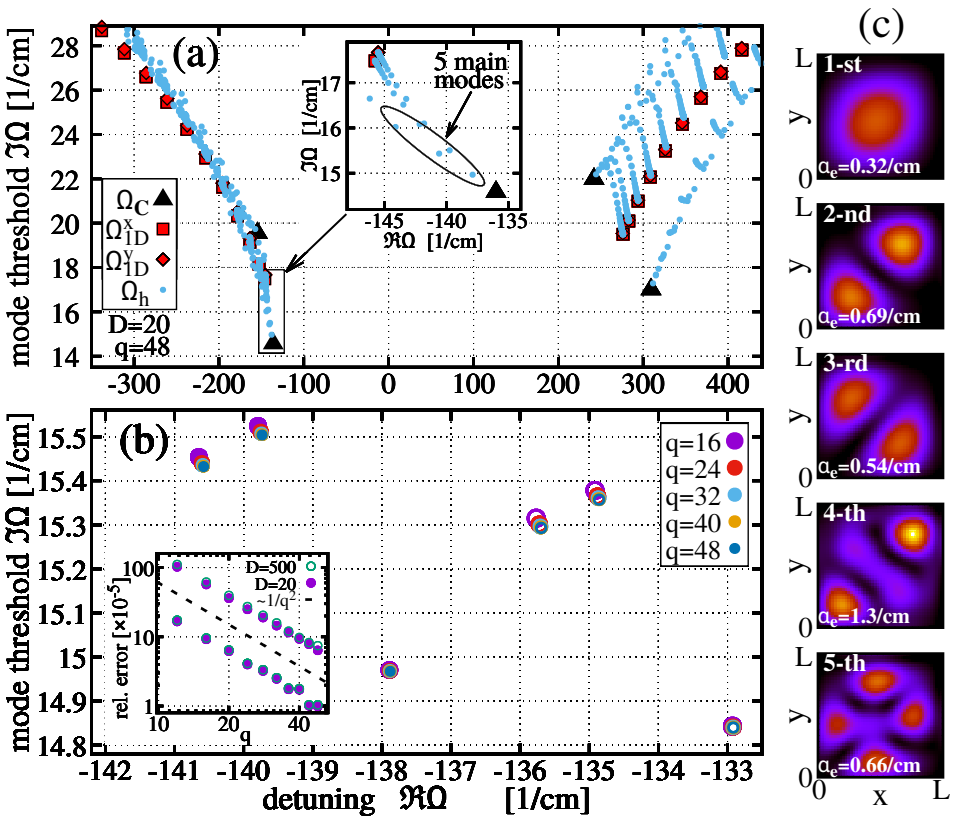

Figure 4: (a): Exact eigenfrequencies of Eq. (3) when $L \to \infty$ (black triangles $\Omega_{\mathbf{C}}$) or field cross-coupling terms in $\mathbf{C}$ are omitted (red squares/rhombs $\Omega_{1D}^{x/y}$), and numerically estimated Ω_h of Eq. (9) for $q = 48$ (light blue dots). Inset: surrounding of the lowest threshold modes. (b): dependence of three main Ω_h on q and D (filled/empty bulets: $D = 20$ and 500, respectively). Inset: 2nd order convergence of two main Ω_h with an increase of q. (c): intensity distribution $|\Phi(x, y)|^2$ of five dominant modes, located within the black ellipse in the inset of (a). $L=1$ mm, other parameters as in Figs. 2, 3.

which show the intensity distribution $|\Phi(x, y)|^2$ of these modes. The operation on the main mode, with a single broad, well-centered circular peak of $|\Phi(x, y)|^2$ and a balance between the edge losses and mode seperation is desirable in applications.

To understand numerical errors induced by discretization, we also find the eigenfrequencies of two related systems that can be solved exactly, i.e., do not depend on the domain discretization factor q. Black triangles in Fig. 4(a) are eigenfrequencies $\Omega_{\mathbf{C}}$ of the 4×4-matrix $\mathbf{C}$, which properly represent accumulation points of Ω_h at very large L. Even for moderate $L = 1$ mm used in our example calculations, one can recognize how multiple blue dots (Ω_h) approach the black triangles ($\Omega_{\mathbf{C}}$). Another system that can be treated analytically is obtained by ignoring field cross-coupling in the original system (3), i.e., setting off-diagonal 2×2 blocks of $\mathbf{C}$ to zero. Eq. (3) decouples into two effectively one-dimensional spectral problems, similar to those that arise when considering linear DFB lasers, and can be treated using discretization-independent transfer-matrix-based methods [13]. Red squares and rhombs represent finite sets of eigenfrequencies $\Omega_{1D}^{x,y}$ of this limit case problem in Fig. 4(a). Slight differences between Ω_{1D}^{x} and Ω_{1D}^{y}, see, e.g., inset of panel (a), are due to tiny (in praxis - unavoidable) distortion of the PC feature's symmetry w.r.t. the diagonal of the PC cell which also violates symmetry $\xi_{r,s} = \xi_{s,r}$ for the Fourier coefficients and induces corresponding changes of $\mathbf{C}$. Most of the light blue dots appear in prolonged clusters. For low thresholds, $\Im\Omega_h < 10/\text{cm}$, one side of nearly all

clusters with densely located eigenfrequencies therein is attached to one of the red boxes Ω_{1D}, which suggests a weak cross-coupling of the field components in the related modes. This agreement is degraded for higher thresholds because of discretization-induced numerical dispersion that implies too large damping of the modes having Ω_h far away from zero.

Thus, several main modes of Eq. (3) with a low threshold $\Im\Omega$ can be properly estimated even with coarse numerical mesh defined by a small factor q. The precision of this approximation in dependence on q is further analyzed in Fig. 4(b). The filled bullets in this diagram represent three lowest-threshold modes calculated using different (still small) q, varying it from 16 to 48. For all these q, the eigenfrequencies are not changing significantly; an increase of q implies some shifts, but the magnitude of these shifts decreases with the growth of q. 2nd and 3rd modes have more pronounced shifts, which agrees with our previous discussion of numerical dispersion issues. Filled bullets in the inset of the same diagram represent the quadratic decay of the relative error $|\frac{\Omega_h(q)-\Omega}{\Omega}|$ for two main modes. For convenience, the inset is drawn using log-log scaling of both axes. The dashed line, which is proportional to $\frac{1}{q^2} = h^2$, shows the expected second-order convergence rate. "Exact" Ω in the relative error formula was estimated by extrapolating the shift of calculated $\Omega_h(q)$ for $q \to \infty$.

At least in the considered example, the discretization step-induced error is small when comparing it to matrix $\mathbf{C}$-truncation-induced changes. This is shown in Fig. 4(b) and its inset, where filled and empty bullets represent eigenfrequencies of the problems constructed using truncated matrices $\mathbf{C}_{2D}^{(D)}$ with $D = 20$ and 500, respectively. Shifts of bullets in panel (b) show that real and imaginary parts of q-induced absolute errors of $\Omega_h(q)|_{q\geq 12}$ in both cases do not exceed $(0.0057, 0.021)/\text{cm}$ for the main mode and about seven-fold values for the second and third modes. On the contrary, the parameter D induced changes of three main Ω_h vary between $(0.128, 4.877)/\text{cm}$ and $(0.147, 4.965)/\text{cm}$, similar to $(0.118, 4.995)/\text{cm}$ dislocation of the lowest threshold $\Omega_{\mathbf{C}}$ shown in the inset of Fig. 3. On the other hand, the mode landscape in Fig. 4(a) and the relations between the main eigenfrequencies Ω_h calculated for $D = 20$ and 500 are almost preserved, which suggests that a constant contribution to real and imaginary parts of $\overline{\Delta\beta}$ can nearly compensate the differences induced by the selection of small parameter D.

5 Parameter study

Finally, we use our algorithms and code for numerical parameter continuation experiments to receive quick information about the PCSEL structures considered. Fig. 5 summarizes the main mode calculations of in Fig. 4 considered PCSEL with different size factors L, varying from $100\,\mu$m up to $3\,$mm ($D = 20$ and $q = 32$ in this case). Since the vertical configuration is unchanged, the matrix $\mathbf{C}$ should be constructed only once during the initiation step. We are interested in PCSEL configurations with low threshold gain of the main mode, see black bullets panel (a), low losses α_{e} at the lateral edges of PCSEL, panel (c), and large threshold separation to the remaining modes, panel (d). In panel (b), we also show shifts of $\Im\Omega$ for considered five modes with the increase of L. Due to insufficient field coupling in small emission area ($L \leq 0.2\,$mm) PCSELs with no reflections at the lateral borders, the mode threshold and corresponding losses α_{e} are huge, and the mode intensity $|\Phi(x, y)|^2$ is concentrated at the lateral borders of the domain. Such PCSEL configurations are useless; the switching-on performance of these devices can be compared with that of short edge-emitting DFB diodes with weak coupling and antireflective coating of the facets. Excellent operation of similar-sized PCSELs discussed in Refs. [9, 10] could be achieved because of a much larger refraction index contrast between the surrounding semiconductor material and the air-filled features in the elementary PC cells. With an increase of L, the main mode's eigenfrequency Ω (black bullets in panels (a) and (b)) rapidly

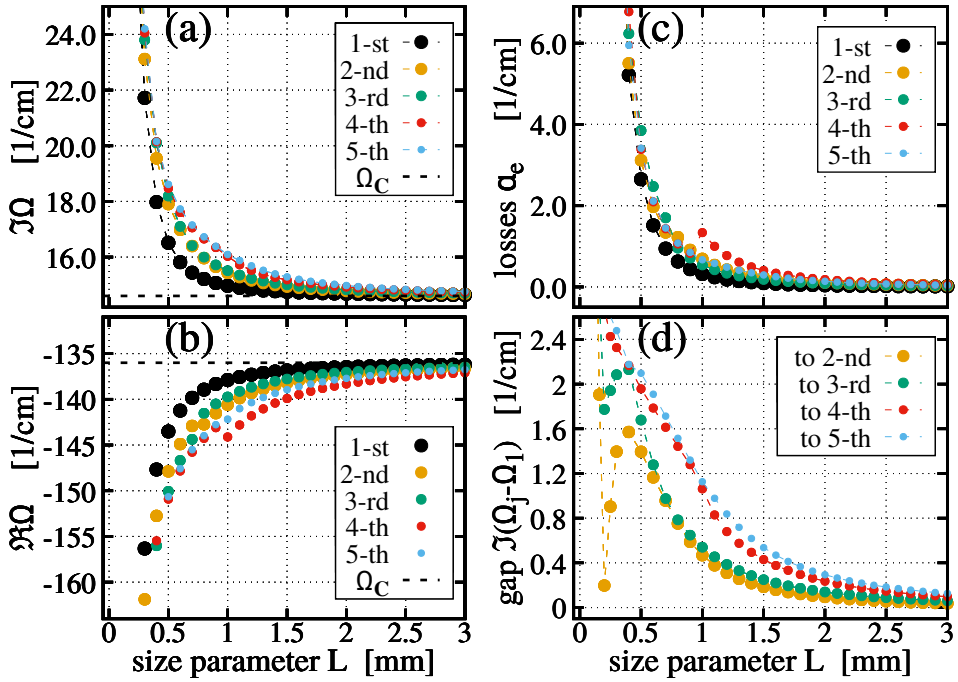

Figure 5: Threshold $\Im\Omega$ (a), detuning $\Re\Omega$ (b), and losses α_e (c) of the five main modes, and the threshold separation $\Im(\Omega_j - \Omega_1)$ between the fundamental (first) and the remaining four higher-order modes (d) as functions of the size factor L. Dashed lines in (a), (b): lowest threshold mode $\Omega_{\mathbf{C}}$ of $\mathbf{C}$. $D = 20$, $q = 32$, while other parameters as in Fig. 4.

approaches the lowest threshold band-edge mode $\Omega_{\mathbf{c}}$ (horizontal lines in the same panels). Loss α_e, panel (c), decreases as well and is below 0.1/cm for $L \geq 1.5$ mm. Unfortunately, the threshold gap (panel (d)) decays with increasing L as well, which is due to the accumulation of eigenfrequencies Ω at $\Omega_{\mathbf{c}}$ in the large L limit. Thus, at very large L, one can expect multimode emission with suboptimal beam characteristics.

In the last example, we performed a similar continuation of L assuming the PCSEL configuration with vertically tilted side walls of features within the PC layer [6]. Such PC layers can be designed intentionally but also unintentionally induced by material etching/regrowth procedures. Thus, such simulations can be helpful when testing the robustness of selected structures to minor technology imperfections. To perform simulations, we subdivided the (previously sole) PC layer into 15 sublayers, assuming that the central sublayer has isosceles right triangle features with $0.8a$-short legs, Fig. 2(a), considered in all previous examples. We linearly changed the triangle leg size across the whole PC layer, such that at the bottom/top sublayers, it was $0.7a/0.9a$ (up-taper) or $0.9a/0.7a$ (down-taper). Such a down-taper configuration in a 3-sublayer PC is shown in Fig. 1. Note that the hypotenuse of the triangular feature in our example still defines an unchanged vertical feature's wall within all PC sublayers. Since n_{eff} for three considered structures was slightly different ($n_{\text{eff}} = 3.3073$, 3.309 and 3.3059 for PCSELs with uniform, up- and down-tapered PC features, respectively), we have also adapted the corresponding PC cell size $a = \lambda_0/n_{\text{eff}}$.

The calculations of the main mode are presented in Fig. 6. Besides both tapered feature configurations, here we show again the modes of an above-studied PCSEL with vertically uniform PC cells (black bullets). Compared to the uniform-feature PCSEL, lasers with down-tapered features (orange) have reduced $\Im\Omega_{\mathbf{c}}$, see triangles in panel (d), and, consequently, reduced thresholds of the main mode, panel (a). The edge losses and gain gap are also slightly improved; cf. orange and black bullets

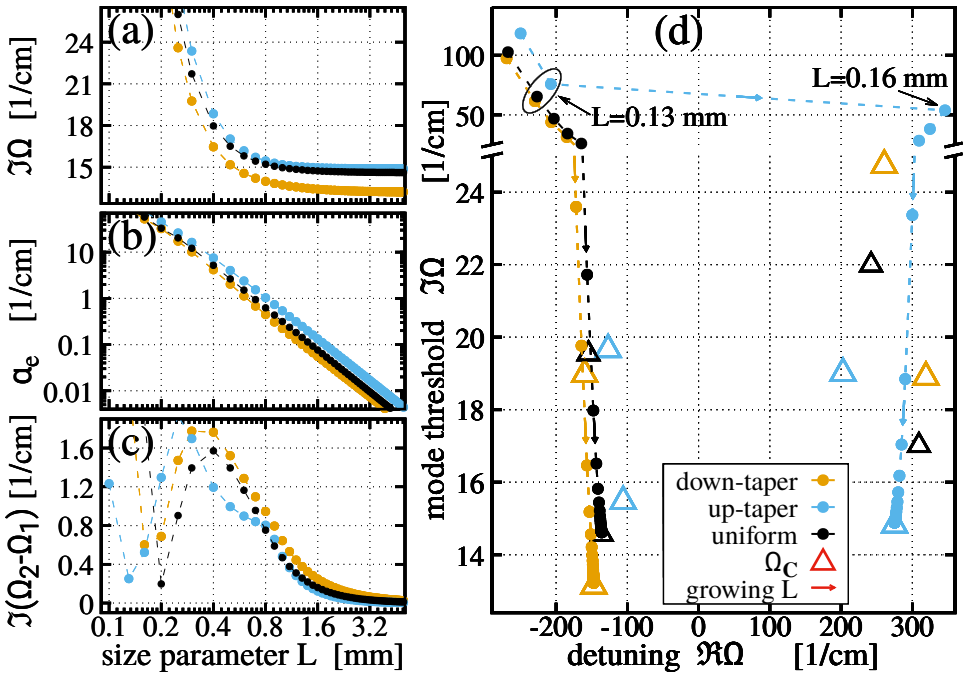

Figure 6: Main modes of PCSELs with down-tapered (orange), up-tapered (light blue), and uniform (black) PC features. Threshold $\Im\Omega$ (a), loss α_e (b) of the main mode, and the threshold gap $\Re(\Omega_2 - \Omega_1)$ (c) as functions of L. (d): down-shifts of Ω with increasing L. Triangles: eigenfrequencies $\Omega_\mathbf{C}$.

in panels (b) and (c). The mode landscape (such as in Fig. 4(a), for example) and the locations of the main modes, except of slightly reduced $\Im\Omega$ and increased separation of different stop-band side modes, have no significant differences. On the other hand, in the PCSELs with up-tapered features (light blue), which have only slightly changed mode threshold, loss factor α_e, and threshold gap, cf. light blue and black dots in panels (a)-(c), the mode relations are quite different. In contrast to the previously considered cases, the dominating mode is now located close to the band-edge mode on the other side of the stopband, see down-shifting light blue bullets at the right side of Fig. 6(d). Thus, tapering of PC features can not only cause relatively smooth small-scale shifts of the band edge modes (as, e.g., observed in Fig. 3) and corresponding smooth changes of the mode landscape and the main eigenfrequencies Ω there but also induce a jump to a new group of dominant modes determined by another band edge mode with significantly differing optical frequency.

At $L \approx 0.15$ mm, two different stop-band side modes of the PCSEL with down-tapered PC features have equal thresholds: see the light blue dots at $L = 0.13$ mm and 0.16 mm in panel (d) and rapidly reduced threshold gap at these L in panel (c). Here, an increase of L implies the role exchange for these modes, visible as a "jump" of the main mode over the stopband in Fig. 6(d). All such mode role exchanges are due to different mode sensitivity $\frac{d}{dp}\Im\Omega$ to the change of the considered parameter p (L in our example). Similar (even though on a smaller scale) swaps of the mode roles in Figs. 5 and 6 are represented by small defects of otherwise smooth parameter-depending curves. For example, the light blue curve in Fig. 6(c) and green/orange curves in Fig. 5(b) and (c) show such defects for $L \approx 0.75$ mm, where the second and third modes are swapped; at $L \approx 0.95$ mm in the same panels of Fig. 5 a new mode takes role of the fourth-lowest threshold mode. In Fig. 5(d), the local minimum of the orange curve also indicates the exchanging roles of the modes with the lowest and the second-lowest thresholds at $L = 0.2$ mm. An understanding and controlling the mode shift rates $\frac{d}{dp}\Im\Omega$ with the changes of model parameters could be very helpful when designing the PCSEL configuration and will be discussed elsewhere.

6 Conclusions and outlook

In this work, we have presented analytic-expression-based algorithms for constructing the field coupling matrix of a three-dimensional coupled wave model for PCSELs. Our algorithms bypass computer arithmetic-induced problems when dealing with large and small exponentials; they are fast and exact, in contrast to approximative approaches [6, 9, 16] or procedures based on numerical integration methods. We have also demonstrated how coarse numerical meshes, 2nd-order precision finite difference schemes, and standard spectral solvers provide a good approximation of a few major optical modes in PCSELs with large (several tens of mm^2) emission areas. Once better precision, more modes, or handling of even large PCSELs are required, we suggest higher-order numerical schemes, which can reduce discretization-induced errors by a few orders or more, depending on the mesh step h.

Optical mode calculations and analysis of their properties in this work were performed assuming time independent and uniform in space propagation factor $\Delta\beta$, which is typically the case at the sub-threshold or near-threshold operation of lasers. Close to the threshold, potentially important modes are well distinguished, and the mode with the lowest threshold $\Im\Omega$ determines the emission properties. Even if remaining stationary in time, above threshold $\Delta\beta$ is a spatially distributed function, accounting for the distribution of carrier density (which itself depends on the inhomogeneous injection and carrier hole burning) and temperature, which typically induces enhancement of the refractive index within the lateral region where the field intensity is high (thermal lensing effects). Deviations of $\Delta\beta$ from the spatially uniform state change the mode landscape, implying the mode wavelength shifts towards or from the Bragg condition, causing a reduction or enhancement of the threshold gaps between the main and higher-order modes. As we have shown in this paper, these gaps in large-area PCSELs are reduced, which is due to increasing concentration of eigenfrequencies Ω close to $\Omega_{\mathbf{C}}$ with growing L. A theoretical understanding of (hot cavity) PCSEL operation can be improved by performing complex theoretical analysis and simulations of the dynamical model [10] (Eqs. (1) supplemented with models for gain dispersion, carrier density [11] and temperature [12], for example) along with simulations and analysis of *instantaneously* on $\Delta\beta(x, y, t)$ depending optical modes, their coupling, and changes with time [13].

The numerical examples used in this work assumed a single-lattice PC crystal characterized by a single isosceles right triangle feature within the PC cell and a low-index contrast PC technology. Efforts to scale power and conversion efficiency in large area PCSELs are expected to benefit from the use of more sophisticated PC designs, for example, as discussed in Ref. [8]. The newly developed numerical tool provides sufficient precision and provides solutions with short calculation times, so that design development can proceed rapidly, especially when laser operation is properly included. A key challenge remains designing large area PCSELs with enhanced threshold gap between the main and the higher-order modes, which would remain robust w.r.t. technology-induced misalignments and laser operation-induced shaping of $\Delta\beta(x, y)$.

References

[1] M.S. Zediker and E.P. Zucker, “High-power diode laser technology XX: a retrospective on 20 years of progress,” in *Proc. SPIE*, vol. 11983, art.no. 1198302, 2022, doi: 10.1117/12.2615260

[2] M. Wilkens, H. Wenzel, J. Fricke, A. Maaßdorf, P. Ressel, S. Strohmaier, A. Knigge, G. Erbert, and G. Tränkle, “High-Efficiency Broad-Ridge Waveguide Lasers,” *IEEE Phot. Techn. Letters*, vol. 30, pp. 545–548, 2018, doi: 10.1109/LPT.2018.2801621.

[3] J. E. Boschker, U. Spengler, P. Ressel, M. Schmidbauer, A. Mogilatenko, and A. Knigge, “Stability of ZnSe-Passivated Laser Facets Cleaved in Air and in Ultra-High Vacuum,” *IEEE Photonics Journal*, vol. 14, art.no. 1531606, 2022, doi: 10.1109/JPHOT.2022.3176675

[4] T. Inoue, R. Morita, K. Nigo, M. Yoshida, M. De Zoysa, K. Ishizaki, and S. Noda, “Self-evolving photonic crystals for ultrafast photonics,” *Nat. Communications*, vol. 14, art.no. 50, 2023, doi: 10.1038/s41467-022-35599-2.

[5] M. Yoshida, S. Katsuno, T. Inoue, J. Gelleta, K. Izumi, M. De Zoysa, K. Ishizaki, and S. Noda, “High-brightness scalable continuous-wave single-mode photonic-crystal laser,” *Nature*, vol. 618, pp. 727–732, 2023, doi: 10.1038/s41586-023-06059-8.

[6] C. Peng, Y. Liang, K. Sakai, S. Iwahashi, and S. Noda, “Coupled-wave analysis for photonic-crystal surface-emitting lasers on air holes with arbitrary sidewalls,” *Optics Express*, vol. 19, pp. 24672–24686, 2011, doi: 10.1364/OE.19.024672.

[7] K. Hirose, Y. Liang, Y. Kurosaka, A. Watanabe, T. Sugiyama, and S. Noda, “Watt-class high-power, high-beam-quality photonic-crystal lasers,” *Nature Photonics*, vol. 8, pp. 406–411, 2014, doi: 10.1038/nphoton.2014.75.

[8] T. Inoue, M. Yoshida, J. Gelleta, K. Izumi, K. Yoshida, K. Ishizaki, M. De Zoysa, and S. Noda, “General recipe to realize photonic-crystal surface-emitting lasers with 100-W-to-1-kW single-mode operation,” *Nat. Comm.*, vol. 13, art.no. 3262, 2022, doi: 10.1038/s41467-022-30910-7.

[9] Y. Liang, C. Peng, K. Sakai, S. Iwahashi, and S. Noda, “Three-dimensional coupled-wave analysis for square-lattice photonic crystal surface emitting lasers with transverse-electric polarization: finite-size effects,” *Optics Express*, vol. 20, pp. 15945–15961, 2012, doi: 10.1364/OE.20.015945.

[10] T. Inoue, R. Morita, M. Yoshida, M. De Zoysa, Y. Tanaka, and S. Noda, “Comprehensive analysis of photonic-crystal surface-emitting lasers via time-dependent three-dimensional coupled-wave theory,” *Phys. Rev. B*, vol. 99, art.no. 035308, 2019, doi: 10.1103/PhysRevB.99.035308.

[11] A. Zeghuzi, M. Radziunas, H.-J. Wünsche, J.-P. Koester, H. Wenzel, U. Bandelow, and A. Knigge, “Traveling wave analysis of non-thermal far-field blooming in high-power broad-area lasers,” *IEEE J. Quantum Electron.*, vol. 55, art.no. 2000207, 2019, doi: 10.1109/JQE.2019.2893352.

[12] A. Zeghuzi, H.-J. Wünsche, H. Wenzel, M. Radziunas, J. Fuhrmann, A. Klehr, U. Bandelow, and A. Knigge, “Time-dependent simulation of thermal lensing in high-power broad-area semiconductor lasers,” *IEEE J. Sel. Top. Quantum Electron.*, vol. 25, art.no. 1502310, 2019, doi: 10.1109/JSTQE.2019.2925926.

[13] M. Radziunas, H.-J. Wünsche, “Multisection Lasers: Longitudinal Modes and their Dynamics,” in *Optoelectronic Devices - Advanced Simulation and Analysis*, pp. 121–150, ed. J. Piprek, Springer Verlag, New York, 2005, doi: 10.1007/0-387-27256-9_5.

[14] M. Radziunas, E. Kuhn, H. Wenzel, B. King, and P. Crump, “Calculation of optical modes in large emission area photonic crystal surface-emitting lasers,” in *IEEE Proc. of Int. Conf. on Numerical Simulation of Optoelectronic Devices (NUSOD)*, Turin, Italy, Sep 18-21, pp. 89-90, 2023, doi: 10.1109/NUSOD59562.2023.10273475.

[15] M. Radziunas, E. Kuhn, H. Wenzel, “Solving a spectral problem for large-area photonic crystal surface-emitting lasers,” submitted to *Mathematical Modelling and Analysis*. WIAS-Preprint 3059, 2023, doi: 10.20347/WIAS.PREPRINT.3059.

[16] Y. Liang, C. Peng, K. Sakai, S. Iwahashi, and S. Noda, “Three-dimensional coupled-wave model for square-lattice photonic crystal lasers with transverse electric polarization: A general approach,” *Phys. Rev, B*, vol. 84, art.no. 195119, 2011, doi: 10.1103/PhysRevB.84.195119.

[17] J. Chilwell and I. Hodgkinson, “Thin-films field-transfer matrix theory of planar multilayer waveguides and reflection from prism-loaded waveguides,” *J. Opt. Soc. Am. A*, vol. 1, pp. 742–753, 1984, doi: 10.1364/JOSAA.1.000742.

[18] S. Boldo, C.-P. Jeannerod, G. Melquiond, J.-M. Muller, “Floating-Point Arithmetic,” *Acta Numerica*, vol. 32, pp. 203-290, 2023, doi: 10.1017/S0962492922000101.

[19] J. Bezanson, A. Edelman, S. Karpinski and V.B. Shah, “Julia: A fresh approach to numerical computing,” *SIAM Review*, vol. 59, pp. 65–98, 2017, doi: 10.1137/141000671.